

Unveiling the Intrinsic Alignment of Galaxies with Self-Calibration and DECaLS DR3 data

Ji YAO ¹, HUANYUAN SHAN,² PENGJIE ZHANG,^{1,3,4} JEAN-PAUL KNEIB,^{5,6} AND ERIC JULLO⁶

¹*Department of Astronomy, Shanghai Jiao Tong University, Shanghai 200240, China*

²*Shanghai Astronomical Observatory (SHAO), Nandan Road 80, Shanghai 200030, China*

³*Tsung-Dao Lee Institute, Shanghai Jiao Tong University, Shanghai 200240, China*

⁴*Shanghai Key Laboratory for Particle Physics and Cosmology, China*

⁵*Institute of Physics, Laboratory of Astrophysics, Ecole Polytechnique Fédérale de Lausanne (EPFL), Observatoire de Sauverny, 1290 Versoix, Switzerland*

⁶*Aix-Marseille Univ, CNRS, CNES, LAM, Marseille, France*

Submitted to ApJ

ABSTRACT

Galaxy intrinsic alignment (IA) is both a source of systematic contamination to cosmic shear measurement and its cosmological applications, and a source of valuable information on the large scale structure of the universe and galaxy formation. The self-calibration (SC) method (Zhang 2010a) was designed to separate IA from cosmic shear, free of IA modeling. It was first successfully applied to the KiDS450 and KV450 data (Yao et al. 2019b). We apply the SC method to the DECaLS DR3 shear + photo-z catalog and significantly improve the IA detection to $\sim 20\sigma$. We find a strong dependence of IA on galaxy color, with strong IA signal for red galaxies, and weak/vanishing IA signal for blue galaxies. The detected IA for red galaxies is in reasonable agreement with the non-linear tidal alignment model and the inferred IA amplitude increases with redshift. We discuss various caveats and possible improvements in the measurement, theory and parameter fitting that will be addressed in future works.

Keywords: cosmology, gravitational lensing: weak, observations, large-scale structure of the universe, galaxy

1. INTRODUCTION

For many cosmological probes, systematic errors in either observation or theory or both are becoming the dominant source of errors. They may already be responsible for several tensions in cosmology, such as the H_0 tension (Riess et al. 2019; Planck Collaboration et al. 2018; Bernal et al. 2016; Lin et al. 2019; Freedman et al. 2019). Another example is the $S_8 = \sigma_8(\Omega_m/0.3)^{\alpha \sim 0.5}$ tension, between the Planck CMB experiment (Planck Collaboration et al. 2018) and the stage III cosmic shear surveys such as KiDS (Kilo Degree Survey, Hildebrandt et al. (2017, 2018)), DES (Dark Energy Survey, Troxel et al. (2017)), and HSC (Hyper Suprime-Cam, Hamana et al. (2019); Hikage et al. (2019)). A variety of tests

have been carried out in investigating the S_8 tension (e.g. Asgari et al. (2019); Troxel et al. (2018); Chang et al. (2019); Joudaki et al. (2019)).

Among systematic errors in weak lensing cosmology based on cosmic shear measurement, the galaxy intrinsic alignment (IA) is a prominent one. Cosmic shear is extracted from galaxy shapes, with the underlying assumption that the intrinsic galaxy shapes have no spatial correlation. However, this assumption is invalid, since the large scale structure environment induces spatial correlation in the galaxy shapes. In the context of weak lensing, the spatially correlated part in the galaxy shapes (ellipticities) is called IA. It has been predicted by theory/simulations (e.g. Croft & Metzler (2000); Catelan et al. (2001); Crittenden et al. (2001); Jing (2002); Hirata & Seljak (2004); Joachimi et al. (2013); Kiessling et al. (2015); Blazek et al. (2015, 2017); Chisari et al. (2017); Xia et al. (2017)), and detected in observations (e.g. Lee & Pen (2001); Heymans et al. (2004);

Bridle & King (2007); Okumura et al. (2009); Dossett & Ishak (2013); Krause et al. (2016); Kirk et al. (2015); Troxel et al. (2017); Samuroff et al. (2019); Yao et al. (2019b). It is one of the key limiting factors to fully realize the power of weak lensing cosmology (Heavens 2002; Refregier 2003; Hoekstra & Jain 2008; LSST Science Collaboration et al. 2009; Weinberg et al. 2013; Troxel & Ishak 2015; Joachimi et al. 2015; Kilbinger 2015; Mandelbaum 2018).

In cosmic shear data analysis, IA is often mitigated by fitting against an assumed fiducial IA template (Troxel et al. 2017; Hildebrandt et al. 2017, 2018; Hamana et al. 2019; Hikage et al. 2019). In contrast, the Self-Calibration (SC) methods (Zhang 2010a,b) were designed to remove the IA contamination without assumption on the IA model. This model independence is achieved, due to an intrinsic difference between the weak lensing field and the intrinsic alignment field. The former is a 2D (projected) field with a profound source-lens asymmetry, while the later is a statistically isotropic 3D field. The SC2008 method (Zhang 2010a) has been applied to stage IV survey forecasts (Yao et al. 2017, 2019a), while the SC2010 method Zhang (2010b) has been examined in simulation (Meng et al. 2018) and combined with SC2008 in forecast (Yao et al. 2019a). These studies showed that the SC method is generally accurate in IA removal/measurement.

Yao et al. (2019b) first applied the SC2008 method to KiDS450 (Hildebrandt et al. 2017) and KV450 (Hildebrandt et al. 2018) shear catalogs. To implement the SC method and to incorporate with various observational effects such as photo-z errors, Yao et al. (2019b) built a Lensing-IA Separation (LIS) pipeline, and succeeded in the IA detection. To further test the applicability of the SC method, and to improve the IA detection and applications, we apply the same LIS pipeline to the DECaLS (Dark Energy Camera Legacy Survey) DR3 shear catalog (Phriksee et al. 2019). Comparing to the previous work, we have significantly more galaxies and larger sky coverage. We use the photo-z obtained from k-nearest-neighbours (Zou et al. 2019). These improvements result in more significant IA detection, and allow us to reveal more detailed information on IA such as its redshift and color dependence.

This paper is organized as follows. In §2, we briefly describe the SC method and the LIS pipeline. We also describe the theoretical model to compare with. §3 describes the DECaLS DR3 data used for the analysis. §4 presents the main results and §5 discusses further implications and possible caveats. We include more technical details in the appendix.

2. THE SC METHOD AND THE LIS PIPELINE

The observed galaxy shape γ^{obs} contains three components,

$$\gamma^{\text{obs}} = \gamma^G + \gamma^N + \gamma^I. \quad (1)$$

Here the superscript “G” denotes gravitational (G) lensing. The galaxy shape noise has a spatially uncorrelated part which we denote with the superscript “N”, and a spatially correlated part (the intrinsic alignment) which we denote with the superscript “I”. When cross-correlating γ^{obs} with galaxy number density δ_g , the γ^N term has no contribution. The measured correlation will contain two parts,

$$\langle \gamma^{\text{obs}} \delta_g \rangle = \langle \gamma^G \delta_g \rangle + \langle \gamma^I \delta_g \rangle. \quad (2)$$

The first term on the right-hand side of the equation is the (lensing part) Gg correlation, and the second term is the (IA part) Ig correlation. The first step of SC2008 is to separate and measure Ig (and Gg), without resorting to IA modeling. The second step is to convert Ig into the GI term contaminating the measurement of cosmic shear auto-correlation, through a scaling relation found in Zhang (2010a). The current paper is restricted to the first step, since no results on the cosmic shear auto-correlation will be presented here. We focus on the Ig measurement and its application.

2.1. Separating Gg and Ig

For a pair of galaxies, we denote the photo-z of the galaxy used for shape measurement as z_γ^P , and the photo-z of the galaxy used for number density measurement as z_g^P . Both the intrinsic alignment and the galaxy number density fields are statistically isotropic 3D fields. Therefore the $\langle Ig \rangle$ correlation with $z_\gamma^P < z_g^P$ is identical to $\langle Ig \rangle$ with $z_\gamma^P > z_g^P$. Namely, it is insensitive to the ordering of (z_γ^P, z_g^P) pair in redshift space. This holds for both real (spectroscopic) redshift and photometric redshift. In contrast, the lensing correlation requires $z_\gamma > z_g$ for the true redshift (z). Therefore in the photo-z (z^P) space, the $\langle Gg \rangle$ correlation is smaller for the pairs with $z_\gamma^P < z_g^P$, compared with the $z_\gamma^P > z_g^P$ pairs.¹

Therefore we can form two sets of two-point statistics measured from the same data in the same photo-z bin (e.g. the i -th photo-z bin). In terms of the angular power spectrum,

$$C_{ii}^{\gamma g} = C_{ii}^{Gg} + C_{ii}^{Ig}, \quad (3a)$$

$$C_{ii}^{\gamma g}|_S = C_{ii}^{Gg}|_S + C_{ii}^{Ig}. \quad (3b)$$

¹ In the limit of negligible photo-z error, the $\langle Gg \rangle$ correlation vanishes for $z_\gamma^P < z_g^P$ pairs. In reality, photo-z has both scatters and outliers, the $\langle Gg \rangle$ correlation persists even for $z_\gamma^P < z_g^P$ pairs.

Here $C_{ii}^{\gamma g}$ is the galaxy shape-number density angular power spectrum for all pairs, while $C_{ii}^{\gamma g}|_S$ is the one only for pairs with $z_\gamma^P < z_g^P$. According to the above analysis, with this “| $_S$ ” selection, the lensing signal drops from C_{ii}^{Gg} to $C_{ii}^{Gg}|_S$, while the IA signal C_{ii}^{Ig} remains the same.

The drop in the lensing signal can be determined by the Q parameter,

$$Q_i(\ell) \equiv \frac{C_{ii}^{Gg}|_S(\ell)}{C_{ii}^{Gg}(\ell)}. \quad (4)$$

$Q(\ell)$ has only weak dependence on cosmology and ℓ (Zhang 2010a; Yao et al. 2017). This makes the SC method cosmology-independent to good accuracy. But it is sensitive to the photo- z quality. $Q = 1$ for perfect photo- z , $Q \rightarrow 0$ for poor photo- z , and $Q \in (0, 1)$ in general. We are then able to separate Gg and Ig (Zhang 2010a; Yao et al. 2019b),

$$C_{ii}^{Gg}(\ell) = \frac{C_{ii}^{\gamma g}(\ell) - C_{ii}^{\gamma g}|_S(\ell)}{1 - Q_i(\ell)}, \quad (5)$$

$$C_{ii}^{Ig}(\ell) = \frac{C_{ii}^{\gamma g}|_S(\ell) - Q_i(\ell)C_{ii}^{\gamma g}(\ell)}{1 - Q_i(\ell)}. \quad (6)$$

SC can be extended to the correlation function straightforwardly. We have

$$w_{ii}^{\gamma g}(\theta) = w_{ii}^{Gg}(\theta) + w_{ii}^{Ig}(\theta), \quad (7a)$$

$$w_{ii}^{\gamma g}|_S(\theta) = w_{ii}^{Gg}|_S(\theta) + w_{ii}^{Ig}(\theta), \quad (7b)$$

and

$$w^{Gg}(\theta) = \frac{w^{\gamma g}(\theta) - w^{\gamma g}|_S(\theta)}{1 - Q_i(\theta)}, \quad (8a)$$

$$w^{Ig}(\theta) = \frac{w^{\gamma g}|_S(\theta) - \bar{Q}_i w^{\gamma g}(\theta)}{1 - Q_i(\theta)}. \quad (8b)$$

Since $Q(\ell)$ is nearly scale-independent, we have $Q_i(\ell) \simeq Q_i(\theta) \simeq \bar{Q}_i$. Namely we can replace $Q_i(\ell)$ ($Q_i(\theta)$) with the mean value \bar{Q}_i . Both $w^{\gamma g}$ and $w^{\gamma g}|_S$ are direct observables and Q_i can be robustly calculated given photo- z PDF, so we are able to separate and measure both w^{Gg} and w^{Ig} . A key step in our method is to calculate Q . The calculation is straightforward, but technical. We present detailed description in the appendix.

2.2. Interpreting the separated Gg and Ig

The next step is to extract the physics out of the Gg and Ig separated above. We need to compare with the theoretically predicted w^{Gg} and w^{Ig} . In this section, we briefly describe the basic theory of weak lensing and intrinsic alignment. The comparison between theory and observation will be presented in §4.

The lensing-galaxy cross power spectrum is calculated by the Limber equation,

$$C_{ii}^{Gg}(\ell) = \int_0^\infty \frac{W_i(\chi)n_i(\chi)}{\chi^2} b_g P_\delta \left(k = \frac{\ell}{\chi}; \chi \right) d\chi. \quad (9)$$

Here W_i is the lensing efficiency function. For a flat universe,

$$W_i(\chi_L) = \frac{3}{2} \Omega_m \frac{H_0^2}{c^2} (1+z_L) \int_{\chi_L}^\infty n_i(\chi_S) \frac{(\chi_S - \chi_L)\chi_L}{\chi_S} d\chi_S. \quad (10)$$

$n_i(\chi)$ is the galaxy distribution of the i^{th} photo- z bin in the comoving distance space, and is linked to the galaxy distribution in the true redshift space by $n_i(\chi) = n_i(z)dz/d\chi$. Here χ is the comoving distance, b_g is the galaxy bias, and P_δ is the matter power spectrum. Similarly, the IA-galaxy cross angular power spectrum C^{Ig} is given by

$$C_{ii}^{Ig}(\ell) = \int_0^\infty \frac{n_i(\chi)n_i(\chi)}{\chi^2} b_g P_{\delta, \gamma^I} \left(k = \frac{\ell}{\chi}; \chi \right) d\chi. \quad (11)$$

In this expression, P_{δ, γ^I} is the 3D matter-IA power spectrum, which depends on the IA model being used (or the “true” IA model). For comparison, we adopt the non-linear tidal alignment model (Catelan et al. 2001; Hirata & Seljak 2004) as the fiducial IA model. It is widely used in the other stage III surveys (Hildebrandt et al. 2017, 2018; Troxel et al. 2017; Hikage et al. 2019; Hamana et al. 2019; Chang et al. 2019). In this model,

$$P_{\delta, \gamma^I} = -A_{\text{IA}}(L, z) \frac{C_1 \rho_{m,0}}{D(z)} P_\delta(k; \chi), \quad (12)$$

where $\rho_{m,0} = \rho_{\text{crit}} \Omega_{m,0}$ is the mean matter density of the universe at $z = 0$. $C_1 = 5 \times 10^{-14} (h^2 M_{\text{sun}}/\text{Mpc}^{-3})$ is the empirical amplitude found in Bridle & King (2007). In this work we adopt $C_1 \rho_{\text{crit}} \approx 0.0134$ as in Krause et al. (2016); Yao et al. (2019b). $D(z)$ is the linear growth factor normalized to 1 today. $A_{\text{IA}}(L, z)$ is the IA amplitude parameter, which is expected to be luminosity(L)- and redshift(z)-dependent. In this work, we will investigate the possible redshift dependence and the galaxy-type dependence of this A_{IA} parameter.

The theoretical prediction of w^{Gg} and w^{Ig} are then given by the Hankel transformation,

$$w(\theta) = \frac{1}{2\pi} \int d\ell \ell C(\ell) J_2(\ell\theta). \quad (13)$$

Here $J_2(x)$ is the Bessel function of the first kind of order 2. We adopt the CCL library ² (Chisari et al.

² Core Cosmology Library, <https://github.com/LSSTDESC/CCL>

Table 1. The fiducial Λ CDM cosmological parameters adopted in our analysis, which correspond to the best-fit cosmology from KiDS450 (Hildebrandt et al. 2017).

Survey	h_0	$\Omega_b h^2$	$\Omega_c h^2$	n_s	σ_8	w
KiDS450	0.75	0.0223	0.119	1.02	0.826	-1.0

2019) for the theoretical calculations. These results are cross-checked with CAMB³ (Lewis et al. 2000) in previous work (Yao et al. 2019b). The cosmological parameters being used to calculate the theoretical predictions are the best-fit cosmology of KiDS450, as shown in Table 1. The impact from uncertainties in the cosmological parameters on the theoretical predictions is negligible, compared with that from uncertainties in the galaxy bias b_g and the IA amplitude A_{IA} . Also, σ_8 strongly degenerates with b_g in our case and they both enter the estimation of w^{Gg} and w^{Ig} in the same way. Therefore for the purpose of studying IA, it is valid to fix the cosmology.

3. SURVEY DATA

We apply our method to the Dark Energy Camera Legacy Survey (DECaLS) Data Release 3, which is part of the Dark Energy Spectroscopic Instrument (DESI) Legacy Imaging Surveys (Dey et al. 2019). The DECaLS DR3 contains images covering 4300 deg² in g-band, 4600 deg² in r-band and 8100 deg² in z-band. In total 4200 deg² have been observed in all three optical bands. The DECaLS data are processed by Tractor (Meisner et al. 2017; Lang et al. 2014).

The sources from the Tractor catalog are divided into five morphological types. Namely,

1. Point sources (PSF),
2. Simple galaxies (SIMP: an exponential profile with a fixed 0.45" effective radius and round profile),
3. de Vaucouleurs (DEV: elliptical galaxies),
4. Exponential (EXP: spiral galaxies),
5. Composite model (COMP: composite profiles which are de Vaucouleurs and exponential with the same source center).

In this catalog, the sky-subtracted images are stacked in five different ways: one stack per band, one flat Spectral Energy Distribution (SED) stack of each g-, r- and z-band, one red (g-r=1 mag and r-z=1 mag) SED stack of all bands. The sources are kept above the detection limit

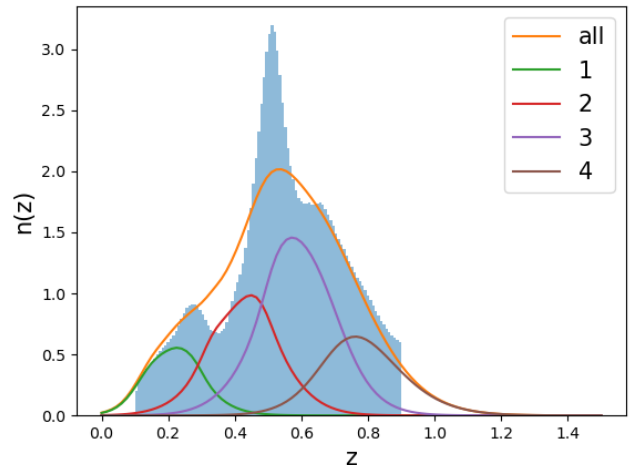


Figure 1. The redshift distribution of the galaxy samples analyzed. The shaded blue histogram is the photo-z distribution. The color curves are the estimated true redshift distributions.

in any stack as candidates. The PSF model (delta function) and the SIMP model are adjusted on individual images, which are convolved by their own PSF model.

The galaxy ellipticities $e_{1,2}$ are free parameters of the above four SIMP, DEV, EXP and COMP models, except for the PSF model. The ellipticity are estimated by a joint fit on the three optical g-, r-, and z-band. We model potential measurement bias with a multiplicative (m) and additive bias (c) (Heymans et al. 2012; Miller et al. 2013; Hildebrandt et al. 2017),

$$\gamma^{\text{obs}} = (1 + m)\gamma^{\text{true}} + c, \quad (14)$$

The additive bias is expected to come from residuals in the anisotropic PSF correction. It depends on galaxy sizes. The multiplicative bias comes from the shear measurement. It can be generated by many effects, such as measurement method (Mandelbaum et al. 2015), blending and crowding (Euclid Collaboration et al. 2019). In order to calibrate our shear catalog, we cross-matched the DECaLS DR3 objects with the Canada-France-Hawaii Telescope (CFHT) Stripe 82 objects, and then computed the correction parameters (Phriksee et al. 2019). In addition, the data from DECaLS DR3 catalog were tested with the Obiwan simulations (Burleigh et al. in prep.).

We employ the photo-z from Zou et al. (2019), which is based on the algorithm of k-nearest-neighbors and local linear regression. Our photo-z is obtained from 5 photometric bands: three optical bands (g, r, and z), and two infrared bands (Wide-field Infrared Survey Explorer

³ Code for Anisotropies in the Microwave Background, <https://camb.info/>

W1 and W2). We use samples with $r < 23$ mag. The training sample includes ~ 2.2 M spectroscopic galaxies.

For each galaxy we use in this work, we add two extra selections. One is to remove some galaxies with extreme shear multiplicative bias (with the cut $1 + m > 0.5$). The other is requiring small estimated photo- z error ($\Delta_z^P < 0.1$). Together with the selection $0.1 < z^P < 0.9$, we obtain 23 million galaxies for the SC analysis. We divide them into 4 photo- z bins ($0.1 < z^P < 0.3$, $0.3 < z^P < 0.5$, $0.5 < z^P < 0.7$ and $0.7 < z^P < 0.9$). For each galaxy, our kNN photo- z algorithm also provides an estimation of the photo- z error. We further assume the error distribution of each photo- z is Gaussian. The overall photo- z distribution $n_i^P(z^P)$ and the true- z distribution $n_i(z)$ are shown in Fig. 1.

4. RESULTS

We present the measurement of $w^{\gamma g}$ and $w^{\gamma g}|_S$ in §4.1, Q in §4.2, w^{Gg} and w^{Ig} in §4.3. All the analysis in this work uses Pipeline 1 developed by JY in Yao et al. (2019b). The 2-point correlation functions described in Eq. (15) is performed with TreeCorr⁴ code (Jarvis et al. 2004).

4.1. $w^{\gamma g}$ and $w^{\gamma g}|_S$ measurement

We adopt the following estimator (Mandelbaum et al. 2006; Singh et al. 2017; Yao et al. 2019b) to calculate $w^{\gamma g}$ and $w^{\gamma g}|_S$,

$$w^{\gamma g} = \frac{\sum_{ED} w_j \gamma_j^+}{\sum_{ED} (1 + m_j) w_j} - \frac{\sum_{ER} w_j \gamma_j^+}{\sum_{ER} (1 + m_j) w_j}. \quad (15)$$

Here \sum_{ED} means summing over all the tangential ellipticity (E) - galaxy number counts in the data (D) pairs, \sum_{ER} means summing over all the tangential ellipticity (E) - galaxy number counts in the random catalog (R) pairs. The numerators give the stacked tangential shear weighted by the weight w_j from the shear measurement algorithm of the j^{th} galaxy. The denominators give the normalization considering the number of pairs, the shear weight w_j , and the calibration for shear multiplicative bias $(1 + m_j)$. Here we note that, after normalization with the number of galaxies, the two denominators $\sum_{ED} (1 + m_j) w_j$ and $\sum_{ER} (1 + m_j) w_j$ are generally considered the same at large scale (> 1 Mpc/h) of our interest, as the boost factor (the ratio of these two) is normally considered as 1 (Mandelbaum et al. 2005; Singh et al. 2017).

For the random catalog, we use the DECaLS DR7 random catalog⁵ and fit it into the DECaLS DR3 shear

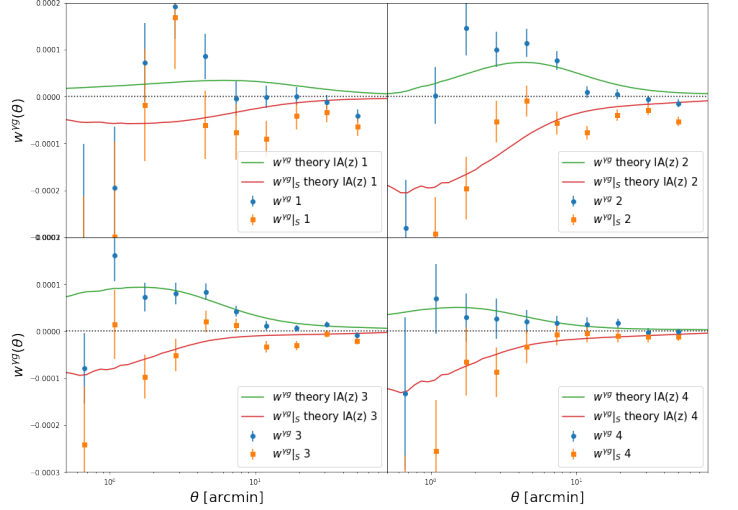


Figure 2. The directly measured $w^{\gamma g}$ (blue dots) and $w^{\gamma g}|_S$ (orange squares), along with the theory curves. The pair weighting adopted in $w^{\gamma g}|_S$ down-weights the lensing contribution while keeps the IA contribution unchanged. The difference between the two then quantifies the efficiency of the SC method. The difference is statistically significant in all 4 redshift bins (3.7σ , 20σ , 15σ , 5.9σ). We note that the theoretical curves are not the best-fit for $w^{\gamma g}$ and $w^{\gamma g}|_S$, but what predicted from the best-fit of separated signals w^{Gg} and w^{Ig} in Fig. 4.

catalog footprint (Phriksee et al. 2019) with Healpy⁶. The size of our random catalog is 10 times the size of the whole DECaLS DR3 shear catalog. This random catalog is used in Eq. (15) for the “R” part, while for the “D” part we use the galaxies in each tomographic bin. So the random sample size is much larger than real data. After the random-subtraction, the null-test with γ^X (the 45 deg rotation of γ^+) of Eq. (15) is consistent with zero.

We note that we are not including the sky varying survey depth in the random sample, for three reasons. (1) Since our photo- z sample has a cut with $r < 23$ (Zou et al. 2019) to maintain high galaxy completeness, the “fake overdensity” due to this effect is expected to be low (Raichoor et al. 2017). (2) The “fake overdensity” due to varying observational depth is expected to have no correlation with the galaxy shapes, as both the lensing part and the IA part are parts of the large scale structure, and are uncorrelated with observational effects. (3) Even if there still exists a selection-induced bias in the 2-point statistics, it should be captured by our Jackknife re-sampling and is therefore appropriately included in the covariance matrix.

⁴ <https://github.com/rmjarvis/TreeCorr>

⁵ <https://legacysurvey.org/dr7/files/>

⁶ <https://github.com/healpy/healpy>

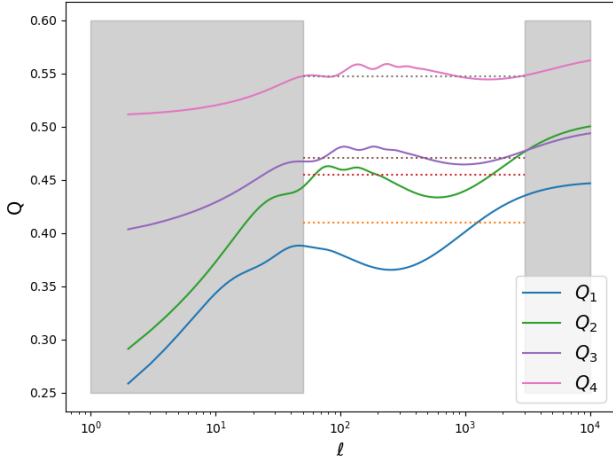


Figure 3. The measured Q_i as a function of multiple ℓ . We are only interested in the region $50 < \ell < 3000$ of most cosmological interest, and therefore we disregard the rest (gray shaded regions). The dotted lines are the approximation $\bar{Q}_i = \langle Q_i(\ell) \rangle$. The applicability of this assumption is discussed in multiple places in the main text.

We use Jackknife re-sampling to obtain the covariance matrices of $w^{\gamma g}$, $w^{\gamma g}|_S$, and the derived w^{Gg} and w^{Ig} . We use a K-means clustering code `kmeans_radec`⁷ and generate 50 Jackknife regions. The choice of 50 Jackknife regions is based on the analysis of Mandelbaum et al. (2006) for 10 angular bins of each photo-z bin.

Fig. 2 shows the measured $w^{\gamma g}$ and $w^{\gamma g}|_S$. The observed $w^{\gamma g}$ and $w^{\gamma g}|_S$ at all four redshift bins are statistically different, with $3.7 - 20\sigma$ significance. It suggests that the photo-z quality is reasonably good, the selection $z_\gamma^P < z_g^P$ is efficient to reduce the lensing contribution. This clear separation is a necessary condition for our SC method.

The $w^{\gamma g} - w^{\gamma g}|_S$ separation is clearly more significant in this work, than in Yao et al. (2019b), which used KiDS450 and KV450 data. This we think is mainly due to the larger galaxy number in our DECaLS sample, especially in the second and the third redshift bins. Differences in the photo-z algorithm adopted and the resulting photo-z quality may also matter. However, since we lack robust information on photo-z outliers to quantify its impact on SC, we leave this issue for further study.

We also show the theoretical curves in Fig. 2. This demonstrates that the nonlinear tidal alignment model can provide a reasonably good description of the measurement.

Nevertheless, we caution that they are not the best theory fit for $w^{\gamma g}$ and $w^{\gamma g}|_S$, but the prediction of the best theory fit for w^{Gg} and w^{Ig} , which we will discuss in the next subsection. The two data sets are identical if we have perfect knowledge of Q . In this work, we choose to fit against w^{Gg} and w^{Ig} , since their physical meanings (the lensing-galaxy correlation and the IA-galaxy correlation) are more straightforward, compared with $w^{\gamma g}$ and $w^{\gamma g}|_S$. But in the analysis, we neglect the weak scale-dependence in Q_i (see Fig. 3 for the values) and we have to test this approximation. The reasonably good agreement (Fig. 2) show that, at least for the current data, the scale-independent Q approximation is valid and the two data sets ($(w^{\gamma g}, w^{\gamma g}|_S)$ versus (w^{Gg}, w^{Ig})) are basically identical. In the future analysis, we need to consider measurement and theory uncertainties in Q , and will use $w^{\gamma g}$ and $w^{\gamma g}|_S$ directly for the fitting. For such exercise, we also need the covariance matrix of the two sets of observables. We discuss them in the Appendix B and Fig. 15 for your interests. As expected, the two have a strong positive correlation, since $w^{\gamma g}|_S$ is totally and positively included in $w^{\gamma g}$. Such a strong correlation must be taken into account in the related data analysis.

4.2. The lensing drop Q_i measurements

Fig. 3 shows the measured lensing drop $Q_i(\ell)$, and we leave calculation details in the appendix A. As we have explained in §2.1, Q is mainly determined by the photo-z quality, with $Q = 0$ for perfect photo-z and $Q = 1$ for totally wrong photo-z. For the SC method to be applicable, Q must be significantly smaller than unity (Zhang 2010a; Yao et al. 2019b). Fig. 3 showed that $Q_i(\ell) \sim 0.5$ for a wide range of ℓ and photo-z bin. Therefore the photo-z quality is already sufficiently good to enable the SC method. Q varies between photo-z bins. We tested that for photo-z outlier rate $< 20\%$, the bias in Q for the current stage surveys is negligible. Besides the difference in photo-z quality, the effective width of the lensing kernel ($W_L(z_S, z_L)$) also plays a role.

According to Fig. 3, as well as in our previous work (Yao et al. 2019b), the Q_i value is roughly constant in the range of $50 < \ell < 3000$. This is the main regime of interest in weak lensing cosmology. Therefore we are able to adopt the approximation $\bar{Q}_i = \langle Q_i(\ell) \rangle$. Inaccuracies arising from this approximation are sub-dominant (with some power shifted between large-scale and small-scale, but not biasing the overall amplitude), comparing to the statistical uncertainties in the final data products w^{Gg} and w^{Ig} . Furthermore, as photo-z quality improves and/or redshift increases, $Q(\ell)$ will become more scale-independent (e.g. Fig. 3 and in Yao et al. (2019b)).

⁷ https://github.com/esheldon/kmeans_radec

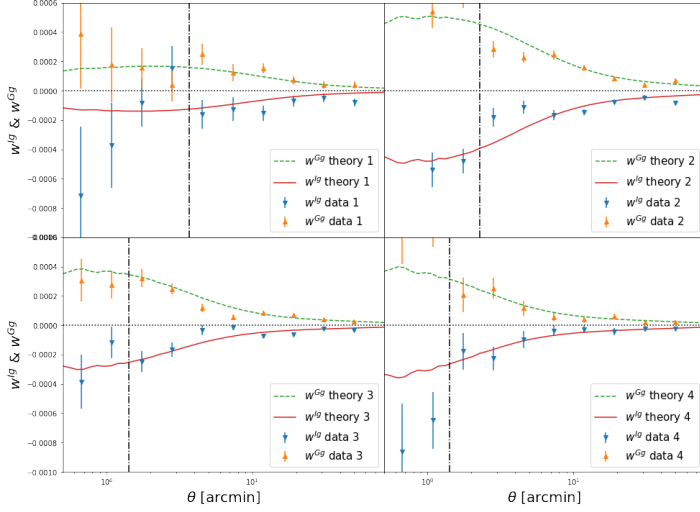


Figure 4. The lensing signal w^{Gg} (orange up-triangles) and the IA signal w^{Ig} (blue down-triangles) measured by the SC method. We also show the best-fit theoretical curves. In the fit, we fix cosmology, but varying the galaxy bias b_g and the IA amplitude A_{IA} for the non-linear tidal alignment model. In the fit, we adopt a small scale cut $r \sim 1$ Mpc (the vertical dash-dot lines).

Nevertheless, we present more discussions about Q_i later within the context of the 2-point correlation functions.

4.3. Lensing-IA separation

With the measured $w^{\gamma g}$, $w^{\gamma g}|_S$ (Fig. 2) and Q_i (Fig. 3), we are then able to separate w^{Gg} and w^{Ig} by Eq. (8a) & (8b). The results are shown in Fig. 4, along with the normalized covariance matrix (Fig. 5). The detection of intrinsic alignment (w^{Ig}) is significant at all four redshift bins and the corresponding S/N=4.7, 17, 8.7, 6.4 respectively.⁸

Now we compare with the theoretical prediction of the nonlinear tidal alignment model. Since the predicted $w^{Ig} \propto b_g A_{IA} P_\delta$, we need to include the measurement $w^{Gg} \propto b_g P_\delta$, in order to break the b_g - A_{IA} degeneracy. Since both w^{Ig} and w^{Gg} are derived from the same set of data, they are expected to have a strong negative correlation. Fig. 5 confirms this expectation of strong anti-correlation. This figure shows

⁸ We caution that the detection significance is likely overestimated, since we do not include uncertainties in the Q value. The induced fluctuation is $\delta w^{Ig} = -w^{Gg} \delta Q / (1 - Q) \simeq -w^{Gg} \times (2\delta Q)$. Since $w^{Ig} \sim w^{Gg}$ for the full sample, the induced fractional error is $\delta w^{Ig} / w^{Ig} \sim -2\delta Q$. The statistical Q fluctuation estimated by the Jackknife method is $\sim 10^{-3}$, and is therefore negligible in the w^{Ig} error budget. However, systematic error of Q arising from photo-z outliers may be larger. Unless $|\delta Q| \gtrsim 0.05$, the detection significance of w^{Ig} will not be significantly affected. After we have reliable estimation on photo-z outliers, we will quantify its impact.

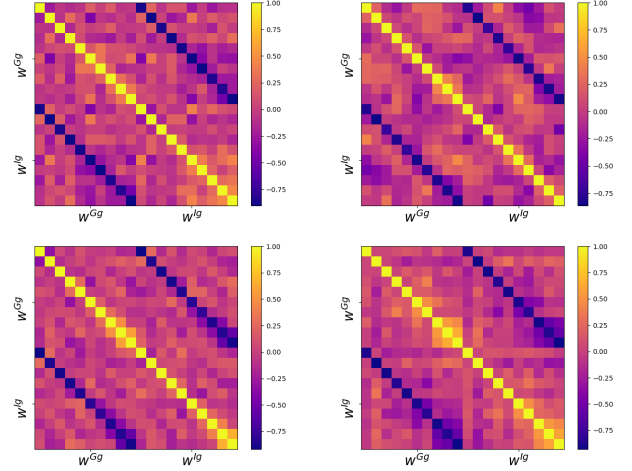


Figure 5. The normalized covariance matrix (The cross correlation coefficient) of the data vector $\mathbf{D} = (w^{Gg}(\theta), w^{Ig}(\theta))$. For each photo-z bin, there are 10 θ -bins for w^{Gg} and 10 for w^{Ig} , so the overall size for the data vector is 20, leading to the 20×20 matrices above. Each matrix corresponds to the redshift bin shown in Fig. 4 in the same position. The measured w^{Gg} and w^{Ig} show strong anti-correlation, which must be taken into account for quantifying the measurement significance and theoretical interpretation.

the cross correlation coefficient (normalized covariance matrix), $r_{ab} \equiv \text{Cov}(a, b) / \sqrt{\text{Cov}(a, a) \text{Cov}(b, b)}$. Here $a, b \in (w^{Gg}(\theta_1), w^{Gg}(\theta_2), \dots, w^{Ig}(\theta_1), \dots)$. Therefore we should fit for w^{Gg} and w^{Ig} simultaneously and take this anti-correlation into account. We test that, if we ignore this strong anti-correlation and fit w^{Gg} and w^{Ig} separately, the bestfits do not well reproduce $w^{\gamma g}$ and $w^{\gamma g}|_S$ in Fig. 2.

The theoretical fitting is carried out with a fixed cosmology (Table 1), and a fixed IA model (the nonlinear tidal alignment model). So there are only two free parameters in the fitting, namely the galaxy bias b_g and the IA amplitude A_{IA} . The two contain the leading order information of the measurements since $w^{Gg} \propto b_g$, and $w^{Ig} \propto b_g A_{IA}$. Furthermore, a large fraction of cosmological dependence (in particular σ_8) can be absorbed into b_g since both $w^{Gg} \propto b_g P_\delta$ and $w^{Gg} \propto (b_g P_\delta) \times A_{IA}$. Also for this reason, the constraint on A_{IA} is less cosmology-dependent than that on b_g . Since the major purpose of this work is to study IA, the above simplification in model fitting meets our needs. With future data of significantly improved S/N, we will perform a global fitting with relaxed constraints of cosmology and IA models.

The MCMC fitting results on b_g and A_{IA} are shown in Fig. 6. The best-fit values in this figure are used to

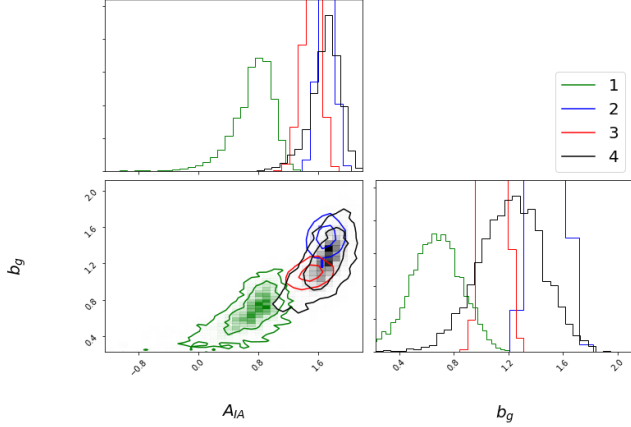


Figure 6. The MCMC fitting results for the galaxy bias b_g and IA amplitude A_{IA} of each photo- z bin. We find a clear redshift-dependent evolution on the IA amplitude A_{IA} . The strong constraining power in bin 2 and 3 are due to their large numbers of galaxies, as shown in Fig. 13. The abnormal behavior of bin 2 is due to the large fraction of red galaxies, which will be discussed later in this work.

plot the best-fit curves in Fig. 2 and 4. The best-fit curves agree with both the lensing signal and the IA signal reasonably well. This suggests that the LIS method works well, and support the non-linear tidal alignment IA model (at least at scale $> \sim 1$ Mpc). Nevertheless, we notice that at the physical scale in between ~ 1 Mpc and ~ 5 Mpc, there exist some discrepancies. This can be seen at $\theta \sim 3$ arcmin for the 2nd redshift bin and $\theta \sim 6$ arcmin for the 3rd redshift bin in Fig. 4. Furthermore, at scales $< \sim 1$ Mpc, corresponding to the angular cut we adopted, the behavior of the lensing signal and the IA signal does not agree with the theoretical curves very well. These could be due to the lack of modeling of the baryonic effects (such as cooling and feedbacks), and scale-dependent and nonlinear b_g at small scales (Xu & Zheng 2018). However, they may also imply IA physics beyond the non-linear tidal alignment model. These are issues for future analysis, with better data.

Fig. 6 shows a clear redshift-dependent on the IA amplitude A_{IA} . When redshift increases, A_{IA} becomes larger. The only exception is the redshift bin 2. This is likely due to larger photo- z scatters and higher red galaxy fraction of the redshift bin 2. We will further discuss it in §4.4.

The S/N in Fig. 4 is higher than that in our previous work (Yao et al. 2019b). This motivates us to further investigate such following questions:

1. How do the IA signals depend on the galaxy color (red/blue galaxies) or other galaxy properties?

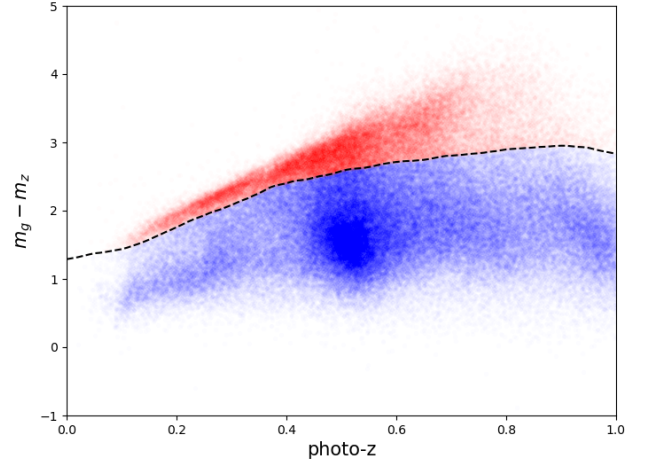


Figure 7. Red-blue galaxy classification through the color-redshift cut (black dashed curve) in the $m_g - m_z$ v.s. z^P space. Table 2 shows the total number of red/blue galaxies

Table 2. The number of red/blue galaxies, in the unit of millions (M).

	$0.1 < z^P < 0.9$	$z1$	$z2$	$z3$	$z4$
Red+Blue	23.4M	2.9M	6.1M	9.7M	4.7M
Red	7.4M	0.8M	2.3M	3.2M	1.1M
Blue	16.0M	2.0M	3.8M	6.5M	3.6M
Red fraction	32%	28%	38%	33%	23%

2. How does the IA amplitude evolves with redshift, for red and blue galaxies?
3. How good is the current non-linear tidal alignment model?

4.4. Separate IA measurements for red and blue galaxies

The galaxy intrinsic alignment is expected to rely on galaxy type, and a major dependence is the galaxy color (red/blue galaxies). Therefore we apply the SC method separately for red and blue galaxies. The classification is done through the estimated clustering effect in the color-redshift space, obtained with the kNN algorithm (Zou et al. 2019). The classification criteria is shown in Fig. 7, with the total number of red/blue galaxies shown in Table 2. The overall red fraction is 32%.

4.4.1. Red galaxies

Fig. 8 shows the separated lensing signal and IA signal for red galaxies, along with the best-fit theoretical curves. The detection of intrinsic alignment (w^{I_g}) for red galaxies is significant at all four redshift bins and the

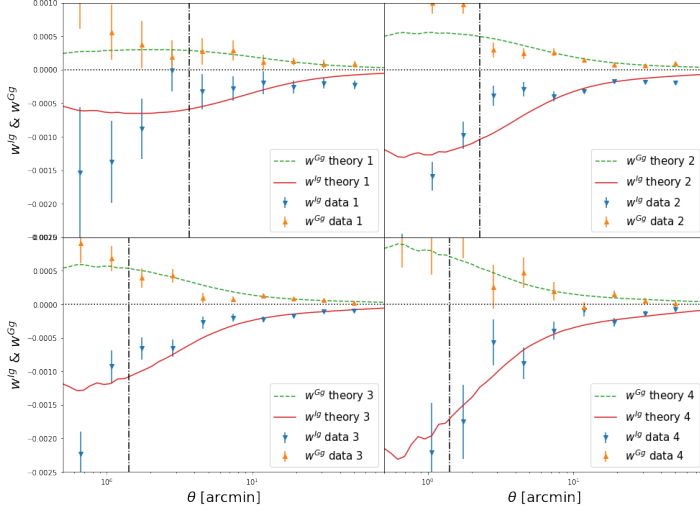


Figure 8. Similar to Fig. 4, but for red galaxies. The joint fit on the galaxy bias b_g and the IA amplitude A_{IA} are shown in Fig. 9, 12 & Table 3.

corresponding $S/N=6.6, 22, 12, 9.2$ respectively. Such S/N is significantly higher than the full sample. This means that blue galaxies included in the full sample contributes little to the IA signal, but induce significant noise and dilute the IA measurement S/N .

Again we achieved good fits for both the lensing part and the IA part. Overall the non-linear tidal alignment model is a good description to the IA of red galaxies. Nevertheless, problems found for the full samples (§4.3) remain for the red samples, since most of the IA signal is contributed by red galaxies. We raise two possibilities responsible for the small scales (< 5 Mpc) problem. (1) The transition between 1-halo term and 2-halo term happens at $1 \sim 10$ Mpc scale. Due to different physics, the IA should be different for the 1-halo term and the 2-halo term. Such complexity is not included in the adopted nonlinear tidal alignment model. (2) At such scales, the impact from higher-order terms such as tidal torquing may become significant (e.g. Blazek et al. (2017)). Careful investigation of these issues, along with better modeling of P_δ and b_g , will be postponed for future study.

Fig. 9, 12 & Table 3 show the constraints of $b_g - A_{IA}$. We see a clear redshift evolution of A_{IA} , namely A_{IA} increases with increasing z . For future cosmic shear or shear cross-correlation studies, it is then important to take this redshift dependence into account.

The second and third redshift bins have similar A_{IA} and b_g . This is largely due to the significant overlap in their real redshift distribution (Fig. 1). Furthermore, the second redshift bin has a higher fraction of red galaxy, leading to a stronger IA signal. These may

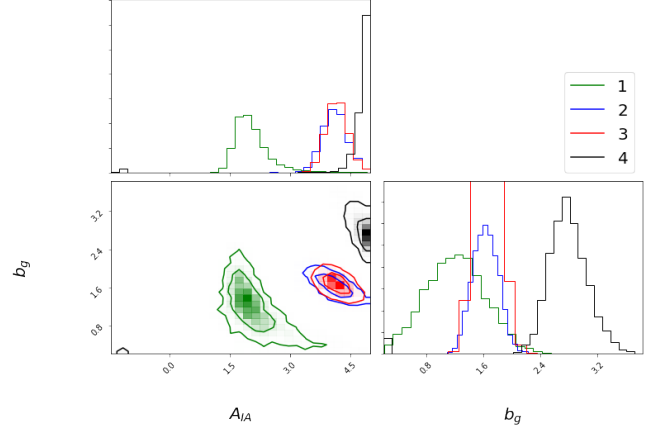


Figure 9. Similar to Fig. 6, but for red galaxies. We find a clear redshift-dependent evolution on the IA amplitude A_{IA} . The overlap for the 2nd and 3rd redshift bins are likely due to significant overlap in their real redshift distribution and higher red galaxy fraction in the second bin.

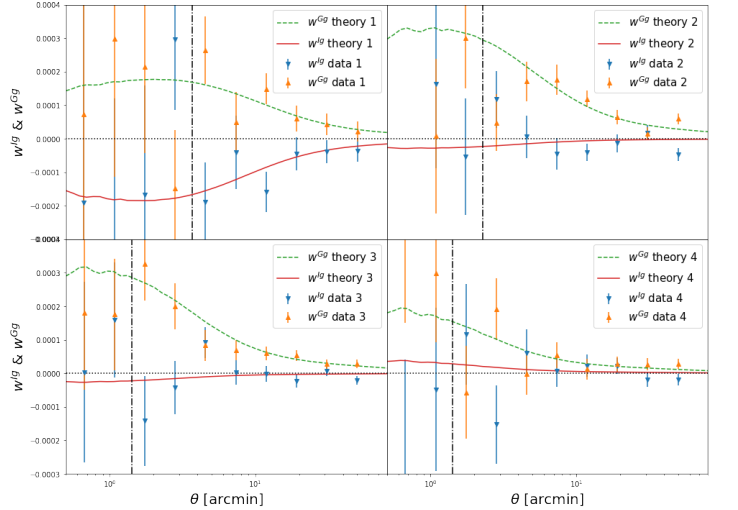


Figure 10. Similar to Fig. 4, but for blue galaxies.

also be responsible for the unusually large A_{IA} of the second redshift bin, for the full galaxy sample (Fig. 6).

4.4.2. Blue galaxies

Fig. 10 presents the separated lensing signal and IA signal, along with their best-fit theoretical curves, for blue galaxies. The b_g and A_{IA} constraints are shown in Fig. 11, 12 & Table 3. Different from the red galaxies, we do not detect the IA signal in bin 2, 3, and 4. This generally agrees with our current understanding that the IA signals mainly exist in the red galaxies. However, we do detect IA signal for blue galaxies in the lowest redshift bin, although the signal is weak. When fitted with the non-linear tidal alignment IA model, the detection significance is $\sim 4\sigma$. The current LIS method can not

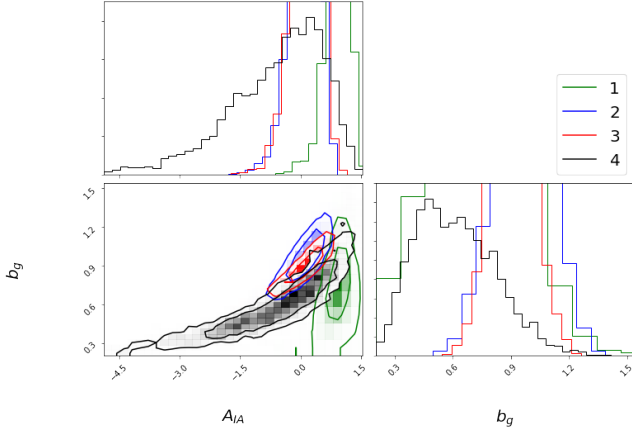


Figure 11. Similar to Fig. 6, but for blue galaxies. Expect for the first redshift bin, A_{IA} are consistent with 0.

fully quantify the impact of photo- z outliers, so the S/N above may be overestimated. Nevertheless, due to the relatively low outlier rate (Zou et al. 2019), we expect an insignificant impact on the estimated S/N. Therefore the detection of non-vanishing IA for the blue galaxy sample defined by Fig. 7 of the lowest redshift bin is statistically significant.

Is this signal caused by the mis-classification of some red galaxies into blue galaxies? To check this possibility, we lower the $m_g - m_z$ cut in Fig. 7 by 0.3, which removes $\sim 20\%$ of the blue galaxies in the first redshift bin. For this “bluer” galaxy sample, we find $A_{IA} = 0.92^{+0.37}_{-0.46}$. The best-fit value remains essentially the same, but the detection significance drops from $\sim 4\sigma$ to $\sim 2\sigma$. The reduction in sample size ($\sim 20\%$) alone is insufficient to explain the $4\sigma \rightarrow 2\sigma$ change. So there may still be contribution from red galaxies (with stronger IA) misidentified as blue galaxies. But the extreme possibility of vanishing IA for blue galaxies is also not supported, otherwise we expect a significant change in the best-fit A_{IA} . One possibility is the existence of a transition phase so that blue galaxies are gaining the tidal alignment type IA, which was conventionally considered as a property of the red galaxies. In this work, we just show this discovery of the IA signal in the low- z blue galaxies. We leave more detailed studies to future work.

5. SUMMARY AND CONCLUSIONS

In this work, we apply the lensing-IA separation (LIS) pipeline of the self-calibration (SC) method to the DECaLS DR3 shear + photo- z catalog. This allows us to measure the galaxy intrinsic alignment signal, free of assumption on the IA model. Therefore the measurement not only reduces IA contaminations in weak lensing cosmology, but also provides valuable information on the physics of IA and galaxy formation. Comparing to our

Table 3. The best-fit A_{IA} and the 1σ error.

A_{IA}	$z1$	$z2$	$z3$	$z4$
Red+Blue	$0.76^{+0.22}_{-0.30}$	$1.70^{+0.10}_{-0.10}$	$1.50^{+0.11}_{-0.12}$	$1.71^{+0.16}_{-0.22}$
Red	$1.96^{+0.45}_{-0.29}$	$4.10^{+0.32}_{-0.31}$	$4.16^{+0.27}_{-0.27}$	$4.86^{+0.10}_{-0.20}$
Blue	$0.95^{+0.20}_{-0.24}$	$0.15^{+0.28}_{-0.38}$	$0.16^{+0.33}_{-0.38}$	$-0.37^{+0.89}_{-1.40}$

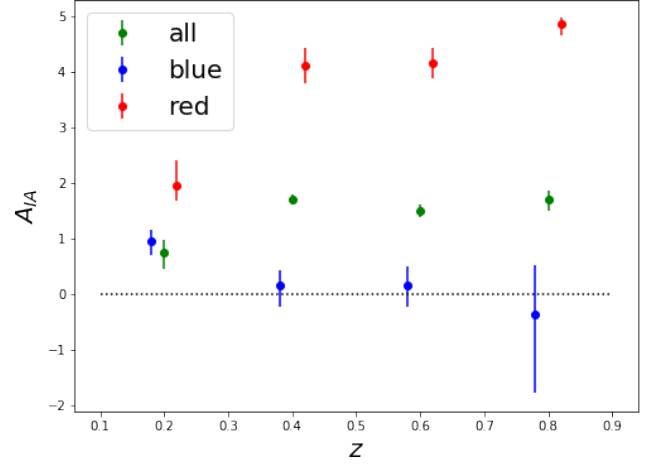


Figure 12. The color- and redshift-dependence of the best-fit A_{IA} .

previous work with the KIDS data (Yao et al. 2019b), we have improved over the following aspects.

- The separation and measurement of lensing and IA are more robust and statistically significant. A crucial diagnostic is the difference in the two direct observables $w^{\gamma g}$ and $w^{\gamma g}|_S$. The difference is improved to more than 20σ for the full galaxy sample.⁹ For this reason, the total detection significance of the IA signal reaches above 17σ .
- We detect the IA dependence on galaxy color. For red galaxies, we detect IA in all photo- z bins at $0.1 < z^P < 0.9$. The detected IA signal shows reasonable agreement with the nonlinear tidal alignment model. For blue galaxies, we detect no IA signal, except for the weak and tentative ($\sim 4\sigma$) detection in the lowest redshift bin at $z^P < 0.3$. The red-blue separation increases the S/N of IA detection in red galaxies to above 23σ .

⁹ If we assume the measurement in four bins are independent, the total detection significance is 27σ . But due to the overlap of galaxies in real redshift space due to photo- z errors, the measurements are partly correlated. The total significance is then between 20σ and 27σ .

Table 4. Goodness of fit (χ^2) to the measured w^{Gg} and w^{Ig} by the nonlinear tidal alignment model. The large χ^2 mainly arises from $\lesssim 5$ Mpc scale (Fig. 4, 8 and 10). They suggest improvement in the theoretical modelling by taking complexities such as baryonic physics, non-linear galaxy bias and beyond tidal alignment IA models into account.

χ^2	z1	z2	z3	z4
Red+Blue	61.3	131.2	75.9	27.8
Red	44.7	241.4	129.7	68.3
Blue	15.5	52.1	44.5	40.1

- We detect the IA dependence on redshift. Especially for red galaxies, the IA amplitude A_{IA} increases with redshift.

The above IA measurements are achieved without assumptions on the IA modeling, due to the nature of the SC method. Together with the high detection significance, we are able to test IA models with these measurements and probe IA physics. As an exercise, we test the nonlinear tidal alignment model against the above data. Table 4 shows the test results for the full/red/blue galaxy samples of four redshift bins. A major finding is the large χ^2 for all data sets, in particular for the second and third redshift bins. Further investigation shows that the large χ^2 values are mainly generated at $1 \sim 5$ Mpc physical scale. This is the transition regime of one-halo and two-halo terms, implying the missing of some physics associated with the transition. Furthermore, smaller scale (< 1 Mpc) data, although not used in the fitting and not included in the best-fit χ^2 , also shows discrepancies with the best-fit theoretical curves. These discrepancies may be caused by missing physics in the tested IA model, baryonic physics in the matter power spectrum P_δ and b_g , or observational effects such as inaccurate photo-z error estimation. We expect

to further investigate these issues with future data, and test the IA physics robustly.

With better data such as DESI imaging survey data release DR8, improved photo-z estimation and shear measurements, we plan to robustly measure the IA amplitude, and its dependence on the physical scale, redshift and galaxy properties such as color and flux. We may also be able to reveal more detailed information, such as the observed negative b_g - A_{IA} correlation in red galaxies, and the possibly positive correlation in blue galaxies (Fig. 9 & 11). This information will be useful to understand galaxy formation. Furthermore, the same analysis also provides the measurement of w^{Gg} , namely the lensing-galaxy cross-correlation free of IA contaminations. This data contains useful information to constrain cosmology, as discussed in the previous work (Yao et al. 2019b). We will present the cosmological studies in separate future works.

6. ACKNOWLEDGEMENTS

The authors thank Hu Zou, Haojie Xu, Jiaxin Wang, Minji Oh, Zhaozhou Li for useful discussions. JY and PZ acknowledge the support of the National Science Foundation of China (11621303, 11433001). HYS acknowledges the support from NSFC of China under grant 11973070, the Shanghai Committee of Science and Technology grant No.19ZR1466600 and Key Research Program of Frontier Sciences, CAS, Grant No. ZDBS-LY-7013.

The codes JY produced for this paper were written in Python. JY thanks all its developers and especially the people behind the following packages: SCIPY (Jones et al. 2001–), NUMPY (van der Walt et al. 2011), ASTROPY (Astropy Collaboration et al. 2013) and MATPLOTLIB (Hunter 2007).

REFERENCES

- Asgari, M., Heymans, C., Hildebrandt, H., et al. 2019, A&A, 624, A134, doi: [10.1051/0004-6361/201834379](https://doi.org/10.1051/0004-6361/201834379)
- Astropy Collaboration, Robitaille, T. P., Tollerud, E. J., et al. 2013, A&A, 558, A33, doi: [10.1051/0004-6361/201322068](https://doi.org/10.1051/0004-6361/201322068)
- Bernal, J. L., Verde, L., & Riess, A. G. 2016, JCAP, 2016, 019, doi: [10.1088/1475-7516/2016/10/019](https://doi.org/10.1088/1475-7516/2016/10/019)
- Blazek, J., MacCrann, N., Troxel, M. A., & Fang, X. 2017, ArXiv e-prints. <https://arxiv.org/abs/1708.09247>
- Blazek, J., Vlah, Z., & Seljak, U. 2015, JCAP, 8, 015, doi: [10.1088/1475-7516/2015/08/015](https://doi.org/10.1088/1475-7516/2015/08/015)
- Bridle, S., & King, L. 2007, New Journal of Physics, 9, 444, doi: [10.1088/1367-2630/9/12/444](https://doi.org/10.1088/1367-2630/9/12/444)
- Catelan, P., Kamionkowski, M., & Blandford, R. D. 2001, MNRAS, 320, L7, doi: [10.1046/j.1365-8711.2001.04105.x](https://doi.org/10.1046/j.1365-8711.2001.04105.x)
- Chang, C., Wang, M., Dodelson, S., et al. 2019, MNRAS, 482, 3696, doi: [10.1093/mnras/sty2902](https://doi.org/10.1093/mnras/sty2902)
- Chisari, N. E., Koukoufilippas, N., Jindal, A., et al. 2017, ArXiv e-prints. <https://arxiv.org/abs/1702.03913>
- Chisari, N. E., Alonso, D., Krause, E., et al. 2019, ApJS, 242, 2, doi: [10.3847/1538-4365/ab1658](https://doi.org/10.3847/1538-4365/ab1658)
- Crittenden, R. G., Natarajan, P., Pen, U.-L., & Theuns, T. 2001, ApJ, 559, 552, doi: [10.1086/322370](https://doi.org/10.1086/322370)

- Croft, R. A. C., & Metzler, C. A. 2000, *ApJ*, 545, 561, doi: [10.1086/317856](https://doi.org/10.1086/317856)
- Dey, A., Schlegel, D. J., Lang, D., et al. 2019, *AJ*, 157, 168, doi: [10.3847/1538-3881/ab089d](https://doi.org/10.3847/1538-3881/ab089d)
- Dossett, J. N., & Ishak, M. 2013, *PhRvD*, 88, 103008, doi: [10.1103/PhysRevD.88.103008](https://doi.org/10.1103/PhysRevD.88.103008)
- Euclid Collaboration, Martinet, N., Schrabback, T., et al. 2019, *A&A*, 627, A59, doi: [10.1051/0004-6361/201935187](https://doi.org/10.1051/0004-6361/201935187)
- Freedman, W. L., Madore, B. F., Hatt, D., et al. 2019, *ApJ*, 882, 34, doi: [10.3847/1538-4357/ab2f73](https://doi.org/10.3847/1538-4357/ab2f73)
- Hamana, T., Shirasaki, M., Miyazaki, S., et al. 2019, arXiv e-prints, arXiv:1906.06041. <https://arxiv.org/abs/1906.06041>
- Heavens, A. F. 2002, in *The Shapes of Galaxies and their Dark Halos*, ed. P. Natarajan, 21–28, doi: [10.1142/9789812778017_0004](https://doi.org/10.1142/9789812778017_0004)
- Heymans, C., Brown, M., Heavens, A., et al. 2004, *MNRAS*, 347, 895, doi: [10.1111/j.1365-2966.2004.07264.x](https://doi.org/10.1111/j.1365-2966.2004.07264.x)
- Heymans, C., Van Waerbeke, L., Miller, L., et al. 2012, *MNRAS*, 427, 146, doi: [10.1111/j.1365-2966.2012.21952.x](https://doi.org/10.1111/j.1365-2966.2012.21952.x)
- Hikage, C., Oguri, M., Hamana, T., et al. 2019, *PASJ*, 71, 43, doi: [10.1093/pasj/psz010](https://doi.org/10.1093/pasj/psz010)
- Hildebrandt, H., et al. 2017, *MNRAS*, 465, 1454, doi: [10.1093/mnras/stw2805](https://doi.org/10.1093/mnras/stw2805)
- Hildebrandt, H., Köhlinger, F., van den Busch, J. L., et al. 2018, arXiv e-prints, arXiv:1812.06076. <https://arxiv.org/abs/1812.06076>
- Hirata, C. M., & Seljak, U. 2004, *PhRvD*, 70, 063526, doi: [10.1103/PhysRevD.70.063526](https://doi.org/10.1103/PhysRevD.70.063526)
- Hoekstra, H., & Jain, B. 2008, *Annual Review of Nuclear and Particle Science*, 58, 99, doi: [10.1146/annurev.nucl.58.110707.171151](https://doi.org/10.1146/annurev.nucl.58.110707.171151)
- Hunter, J. D. 2007, *Computing in Science Engineering*, 9, 90, doi: [10.1109/MCSE.2007.55](https://doi.org/10.1109/MCSE.2007.55)
- Jarvis, M., Bernstein, G., & Jain, B. 2004, *MNRAS*, 352, 338, doi: [10.1111/j.1365-2966.2004.07926.x](https://doi.org/10.1111/j.1365-2966.2004.07926.x)
- Jing, Y. P. 2002, *MNRAS*, 335, L89, doi: [10.1046/j.1365-8711.2002.05899.x](https://doi.org/10.1046/j.1365-8711.2002.05899.x)
- Joachimi, B., Semboloni, E., Hilbert, S., et al. 2013, *MNRAS*, 436, 819, doi: [10.1093/mnras/stt1618](https://doi.org/10.1093/mnras/stt1618)
- Joachimi, B., Cacciato, M., Kitching, T. D., et al. 2015, *SSRv*, 193, 1, doi: [10.1007/s11214-015-0177-4](https://doi.org/10.1007/s11214-015-0177-4)
- Jones, E., Oliphant, T., Peterson, P., et al. 2001–, *SciPy: Open source scientific tools for Python*. <http://www.scipy.org/>
- Joudaki, S., Hildebrandt, H., Traykova, D., et al. 2019, arXiv e-prints, arXiv:1906.09262. <https://arxiv.org/abs/1906.09262>
- Kiessling, A., Cacciato, M., Joachimi, B., et al. 2015, *SSRv*, 193, 67, doi: [10.1007/s11214-015-0203-6](https://doi.org/10.1007/s11214-015-0203-6)
- Kilbinger, M. 2015, *Reports on Progress in Physics*, 78, 086901, doi: [10.1088/0034-4885/78/8/086901](https://doi.org/10.1088/0034-4885/78/8/086901)
- Kirk, D., Brown, M. L., Hoekstra, H., et al. 2015, *SSRv*, 193, 139, doi: [10.1007/s11214-015-0213-4](https://doi.org/10.1007/s11214-015-0213-4)
- Krause, E., Eifler, T., & Blazek, J. 2016, *MNRAS*, 456, 207, doi: [10.1093/mnras/stv2615](https://doi.org/10.1093/mnras/stv2615)
- Lang, D., Hogg, D. W., & Schlegel, D. J. 2014, arXiv e-prints, arXiv:1410.7397. <https://arxiv.org/abs/1410.7397>
- Lee, J., & Pen, U.-L. 2001, arXiv e-prints, astro. <https://arxiv.org/abs/astro-ph/0111186>
- Lewis, A., Challinor, A., & Lasenby, A. 2000, *ApJ*, 538, 473, doi: [10.1086/309179](https://doi.org/10.1086/309179)
- Lin, W., Mack, K. J., & Hou, L. 2019, arXiv e-prints, arXiv:1910.02978. <https://arxiv.org/abs/1910.02978>
- LSST Science Collaboration, Abell, P. A., Allison, J., et al. 2009, arXiv e-prints, arXiv:0912.0201. <https://arxiv.org/abs/0912.0201>
- Mandelbaum, R. 2018, *ARA&A*, 56, 393, doi: [10.1146/annurev-astro-081817-051928](https://doi.org/10.1146/annurev-astro-081817-051928)
- Mandelbaum, R., Hirata, C. M., Ishak, M., Seljak, U., & Brinkmann, J. 2006, *MNRAS*, 367, 611, doi: [10.1111/j.1365-2966.2005.09946.x](https://doi.org/10.1111/j.1365-2966.2005.09946.x)
- Mandelbaum, R., Hirata, C. M., Seljak, U., et al. 2005, *Monthly Notices of the Royal Astronomical Society*, 361, 1287, doi: [10.1111/j.1365-2966.2005.09282.x](https://doi.org/10.1111/j.1365-2966.2005.09282.x)
- Mandelbaum, R., Rowe, B., Armstrong, R., et al. 2015, *MNRAS*, 450, 2963, doi: [10.1093/mnras/stv781](https://doi.org/10.1093/mnras/stv781)
- Meisner, A. M., Lang, D., & Schlegel, D. J. 2017, *AJ*, 154, 161, doi: [10.3847/1538-3881/aa894e](https://doi.org/10.3847/1538-3881/aa894e)
- Meng, X.-g., Yu, Y., Zhang, P., & Jing, Y. 2018, *ApJ*, 864, 1, doi: [10.3847/1538-4357/aad504](https://doi.org/10.3847/1538-4357/aad504)
- Miller, L., Heymans, C., Kitching, T. D., et al. 2013, *MNRAS*, 429, 2858, doi: [10.1093/mnras/sts454](https://doi.org/10.1093/mnras/sts454)
- Okumura, T., Jing, Y. P., & Li, C. 2009, *ApJ*, 694, 214, doi: [10.1088/0004-637X/694/1/214](https://doi.org/10.1088/0004-637X/694/1/214)
- Phriksee, A., Jullo, E., Limousin, M., et al. 2019, arXiv e-prints, arXiv:1910.10983. <https://arxiv.org/abs/1910.10983>
- Planck Collaboration, Akrami, Y., Arroja, F., et al. 2018, arXiv e-prints, arXiv:1807.06205. <https://arxiv.org/abs/1807.06205>
- Raichoor, A., Comparat, J., Delubac, T., et al. 2017, *MNRAS*, 471, 3955, doi: [10.1093/mnras/stx1790](https://doi.org/10.1093/mnras/stx1790)
- Refregier, A. 2003, *ARA&A*, 41, 645, doi: [10.1146/annurev.astro.41.111302.102207](https://doi.org/10.1146/annurev.astro.41.111302.102207)
- Riess, A. G., Casertano, S., Yuan, W., Macri, L. M., & Scolnic, D. 2019, *ApJ*, 876, 85, doi: [10.3847/1538-4357/ab1422](https://doi.org/10.3847/1538-4357/ab1422)

- Samuroff, S., Blazek, J., Troxel, M. A., et al. 2019, MNRAS, 489, 5453, doi: [10.1093/mnras/stz2197](https://doi.org/10.1093/mnras/stz2197)
- Singh, S., Mandelbaum, R., Seljak, U., Slosar, A., & Vazquez Gonzalez, J. 2017, Monthly Notices of the Royal Astronomical Society, 471, 3827, doi: [10.1093/mnras/stx1828](https://doi.org/10.1093/mnras/stx1828)
- Troxel, M. A., & Ishak, M. 2015, PhR, 558, 1, doi: [10.1016/j.physrep.2014.11.001](https://doi.org/10.1016/j.physrep.2014.11.001)
- Troxel, M. A., et al. 2017, ArXiv e-prints. <https://arxiv.org/abs/1708.01538>
- Troxel, M. A., Krause, E., Chang, C., et al. 2018, MNRAS, 479, 4998, doi: [10.1093/mnras/sty1889](https://doi.org/10.1093/mnras/sty1889)
- van der Walt, S., Colbert, S. C., & Varoquaux, G. 2011, Computing in Science and Engineering, 13, 22, doi: [10.1109/MCSE.2011.37](https://doi.org/10.1109/MCSE.2011.37)
- Weinberg, D. H., Mortonson, M. J., Eisenstein, D. J., et al. 2013, PhR, 530, 87, doi: [10.1016/j.physrep.2013.05.001](https://doi.org/10.1016/j.physrep.2013.05.001)
- Xia, Q., Kang, X., Wang, P., et al. 2017, ApJ, 848, 22, doi: [10.3847/1538-4357/aa8d17](https://doi.org/10.3847/1538-4357/aa8d17)
- Xu, X., & Zheng, Z. 2018, MNRAS, 479, 1579, doi: [10.1093/mnras/sty1547](https://doi.org/10.1093/mnras/sty1547)
- Yao, J., Ishak, M., Lin, W., & Troxel, M. A. 2017, ArXiv e-prints. <https://arxiv.org/abs/1707.01072>
- Yao, J., Ishak, M., Troxel, M. A., & LSST Dark Energy Science Collaboration. 2019a, MNRAS, 483, 276, doi: [10.1093/mnras/sty3188](https://doi.org/10.1093/mnras/sty3188)
- Yao, J., Pedersen, E. M., Ishak, M., et al. 2019b, arXiv e-prints, arXiv:1911.01582. <https://arxiv.org/abs/1911.01582>
- Zhang, P. 2010a, ApJ, 720, 1090, doi: [10.1088/0004-637X/720/2/1090](https://doi.org/10.1088/0004-637X/720/2/1090)
- . 2010b, MNRAS, 406, L95, doi: [10.1111/j.1745-3933.2010.00893.x](https://doi.org/10.1111/j.1745-3933.2010.00893.x)
- Zou, H., Gao, J., Zhou, X., & Kong, X. 2019, The Astrophysical Journal Supplement Series, 242, 8, doi: [10.3847/1538-4365/ab1847](https://doi.org/10.3847/1538-4365/ab1847)

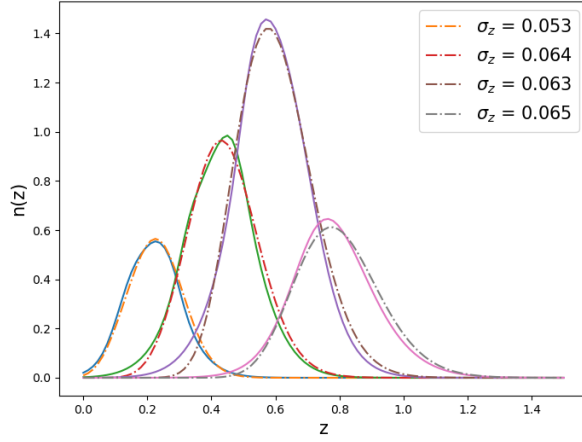


Figure 13. The approximation of uniform photo- z scatter σ_z . The solid curves are the redshift distribution $n_i(z)$ with stacked PDF of all the galaxies in the same redshift bin. They are the same distributions as shown in Fig. 1. The dash-dot curves are using the approximation with a uniform σ_z in each redshift bin. This approximation is to improve the calculation speed of Eq. (A3).

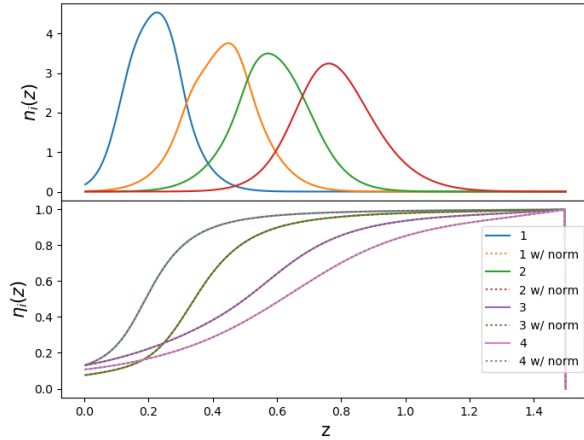


Figure 14. The efficiency function $\eta_i(z)$ (Eq. A3). The solid curves are the $\eta_i(z)$ values directly calculated from Eq. (A3), while the dotted curves are replacing the “2” factor on the numerator of Eq. (A3) with Eq. (A6), demonstrating that this “2” factor is indeed the correct normalization. The upper panel shows the normalized redshift distribution $n_i(z)$. $\eta_i(z)$ has the largest slope near the peak z_i^{peak} of $n_i(z)$. $\eta_i(z) \rightarrow 1$ when $z \gg z_i^{\text{peak}}$, since under such limit S in Eq. (A6) can be replaced by $1/2$.

APPENDIX

A. CALCULATING THE LENSING DROP PARAMETER Q

Q_i plays a crucial role in lensing-IA separation (Eq. (5) & (6)). Theoretically, Q_i is defined by Eq. (4), with C_{ii}^{Gg} given by Eq. (9), and $C_{ii}^{Gg}|_S$ given by

$$C_{ii}^{Gg}|_S(\ell) = \int_0^\infty \frac{W_i(\chi)n_i(\chi)}{\chi^2} b_g P_\delta \left(k = \frac{\ell}{\chi}; \chi \right) \eta_i(z) d\chi. \quad (\text{A1})$$

The extra factor $\eta_i(z)$ arises from the fact that $C^{Gg}|_S$ only contains pairs with $z_\gamma^P < z_g^P$ (Zhang 2010a).

$$\begin{aligned} \eta_i(z) &= \eta_i(z_L = z_g = z), \\ \eta_i(z_L, z_g) &= \frac{2 \int dz_G^P \int dz_g^P \int_0^\infty dz_G W_L(z_L, z_G) p(z_G|z_G^P) p(z_g|z_g^P) S(z_G^P, z_g^P) n_i^P(z_G^P) n_i^P(z_g^P)}{\int dz_G^P \int dz_g^P \int_0^\infty dz_G W_L(z_L, z_G) p(z_G|z_G^P) p(z_g|z_g^P) n_i^P(z_G^P) n_i^P(z_g^P)}. \end{aligned} \quad (\text{A2})$$

Here z_L , z_g and z_G denote the lens redshift, the galaxy redshift, and the lensing source redshift, respectively. The quantities with superscript ‘‘P’’ denote photometric redshifts and the ones without it are the true redshifts z^P . The integral $\int dz_G^P$ and $\int dz_g^P$ are both over $[z_{i,\min}^P, z_{i,\max}^P]$, namely the photo- z range of the i^{th} tomographic bin. The lensing kernel W_L for a flat universe is given by

$$W_L(z_L, z_S) = \begin{cases} \frac{3}{2} \Omega_m \frac{H_0^2}{c^2} (1 + z_L) \chi_L (1 - \frac{z_L}{z_S}) & \text{for } z_L < z_S; \\ 0 & \text{otherwise} \end{cases}; \quad (\text{A3})$$

$p(z|z^P)$ is the redshift probability distribution function (PDF). In reality each galaxy has its own PDF. To speed up the calculation, we approximate it as a Gaussian function identical for all galaxies with the same z^P , as we adopted in the previous work (Yao et al. 2017). $S(z_G^P, z_g^P)$ is the selection function for the ‘‘| $_S$ ’’ symbol,

$$S(z_G^P, z_g^P) = \begin{cases} 1 & \text{for } z_G^P < z_g^P; \\ 0 & \text{otherwise.} \end{cases} \quad (\text{A4})$$

$n_i^P(z^P)$ gives the photo- z distribution function in the i^{th} tomographic bin. The calculation of $\eta(z)$ can be extremely massive, since different galaxies (even with the same z^P) in general have different photo- z PDF. For fast calculation, we follow our previous work (Yao et al. 2017) and assume a uniform Gaussian PDF for all galaxies in the given photo- z bin,

$$p(z|z^P) = \frac{1}{\sqrt{2\pi}\sigma_z(1+z)} \exp\left\{-\frac{(z - z^P - \Delta_z^i)^2}{2[\sigma_z(1+z)]^2}\right\}. \quad (\text{A5})$$

σ_z in the above equation is the averaged photo- z scatter of all galaxies in the given photo- z bin. This approximation is reasonably accurate, since the resulting real redshift distribution $n_i(z)$ is almost identical to the ones by the stacking PDF method (Fig. 13).

We then use the Gaussian photo- z PDF with the averaged scatter σ_z (shown in the labels of Fig. 13) for each redshift bin to calculate $\eta_i(z)$, C^{Gg} and $C^{Gg}|_S$ through Eq. (A3), (9) and (A1). Then finally we obtain the lensing drop $Q_i(\ell)$ for each redshift bin according to Eq. (4). We leave the intermediate step of η_i in the Appendix A and Fig. 14 for your interests. Fig. 14 shows $\eta_i(z)$ of DECaLS DR3, and its dependence on the redshift distribution $n_i(z)$. The factor 2 in Eq. A3 arises from an integral equality theoretically predicted in Zhang (2010a),

$$\frac{\int_{z_{i,\min}^P}^{z_{i,\max}^P} dz_G^P \int_{z_{i,\min}^P}^{z_{i,\max}^P} dz_g^P n_i^P(z_G^P) n_i^P(z_g^P)}{\int_{z_{i,\min}^P}^{z_{i,\max}^P} dz_G^P \int_{z_{i,\min}^P}^{z_{i,\max}^P} dz_g^P n_i^P(z_G^P) n_i^P(z_g^P) S(z_G^P, z_g^P)} = 2. \quad (\text{A6})$$

This is indeed valid, as shown in Fig. 14.

The calculation of $Q_i(\ell)$ requires the photo- z distribution $n_i^P(z^P)$, the true redshift distribution $n_i(z)$, and cosmology (e.g. through P_δ and $W_L(z_L, z_S)$). However, its cosmological dependence is weak, since the cosmology dependent terms enter the same way in both C^{Gg} and $C^{Gg}|_S$ and therefore largely cancel each other in the ratio (Q). For the similar reason, $Q_i(\ell)$ is almost scale-independent, as verified numerically (Yao et al. 2017, 2019a,b). Furthermore, Q will be more scale-independent, with increasing photo- z errors, and higher redshifts accessible to future data. Therefore the Q in the power spectrum SC is essentially the same as the Q in the correlation function SC.

B. COVARIANCE MATRIX FOR THE OBSERVABLES

We show the normalized covariance matrix of $\{w^{\gamma g}(\theta), w^{\gamma g}|_S(\theta)\}$ in Fig. 15. It is obvious that the two observables have a strong positive correlation, simply due to the fact that the data producing $w^{\gamma g}|_S(\theta)$ is completely included in

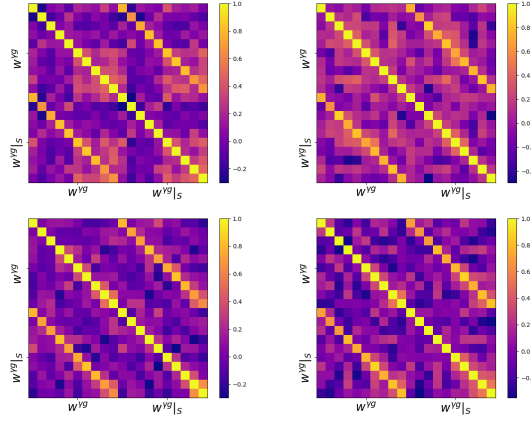


Figure 15. The normalized covariance matrix (the correlation coefficient $r_{ab} = \text{Cov}(a, b) / \sqrt{\text{Cov}(a, a)\text{Cov}(b, b)}$) for the LIS observable data vector $\{w^{\gamma g}(\theta), w^{\gamma g}|_S(\theta)\}$. There are 10 θ -bins for $w^{\gamma g}$ and 10 for $w^{\gamma g}|_S$, so the overall size for the data vector is 20, leading to the 20×20 matrix above. Each matrix correspond to the redshift bin shown in Fig. 2 in the same position. There are strong positive correlation between $w^{\gamma g}$ and $w^{\gamma g}|_S$, important for the data analysis.

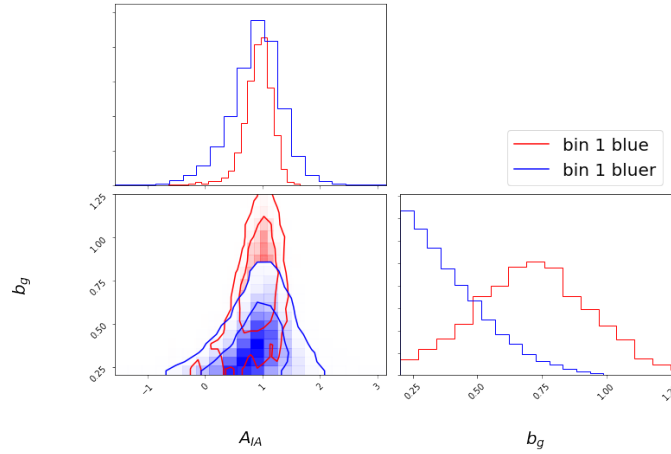


Figure 16. Comparison of the b_g - A_{IA} constraints between the blue galaxy sample and the “bluer” galaxy sample, of redshift bin 1. After throwing away $\sim 20\%$ “redder” galaxies in the “blue” galaxy sample, we found a significant drop in the galaxy bias b_g . However, the tidal alignment IA amplitude remains roughly the same. The physical origin of the weak IA detection in the blue sample needs further investigation.

$w^{\gamma g}(\theta)$. This positive correlation is converted into a negative correlation in the separated w^{Gg} and w^{Ig} (Fig. 5). If uncertainties in Q can be neglected, the above covariance matrix and the covariance matrix of $\{w^{Gg}(\theta), w^{Ig}(\theta)\}$ can be used interchangeably. This is the simplification that we adopt in this paper. However, eventually we need to consider uncertainties in Q (e.g. from photo- z errors), where we should use the covariance matrix of $\{w^{\gamma g}(\theta), w^{\gamma g}|_S(\theta)\}$.

C. BLUER SAMPLE IN BIN 1

Here we test the robustness of the $\sim 4\sigma$ IA detection in the 1st bin of the blue galaxies. By reducing the $m_g - m_z$ red-blue cut by 0.3 and throwing away $\sim 20\%$ of the “redder” samples, we form the “bluer” galaxy sample. The best-fit IA amplitude $A_{\text{IA}, \text{bin1}}^{\text{bluer}} = 0.92^{+0.37}_{-0.46}$, almost identical to the best-fit $A_{\text{IA}, \text{bin1}}^{\text{blue}} = 0.95^{+0.20}_{-0.24}$ before the extra cut. The MCMC results are shown in Fig. 16.